

## Estimation of river flow using CubeSats remote sensing

Junqueira, Adriano M.; Mao, Feng; Mendes, Tatiana S.G.; Simões, Silvio J.C.; Balestieri, José A.P.; Hannah, David M.

DOI:

[10.1016/j.scitotenv.2021.147762](https://doi.org/10.1016/j.scitotenv.2021.147762)

License:

Creative Commons: Attribution-NonCommercial-NoDerivs (CC BY-NC-ND)

*Document Version*

Peer reviewed version

*Citation for published version (Harvard):*

Junqueira, AM, Mao, F, Mendes, TSG, Simões, SJC, Balestieri, JAP & Hannah, DM 2021, 'Estimation of river flow using CubeSats remote sensing', *Science of the Total Environment*, vol. 788, 147762. <https://doi.org/10.1016/j.scitotenv.2021.147762>

[Link to publication on Research at Birmingham portal](#)

### General rights

Unless a licence is specified above, all rights (including copyright and moral rights) in this document are retained by the authors and/or the copyright holders. The express permission of the copyright holder must be obtained for any use of this material other than for purposes permitted by law.

- Users may freely distribute the URL that is used to identify this publication.
- Users may download and/or print one copy of the publication from the University of Birmingham research portal for the purpose of private study or non-commercial research.
- User may use extracts from the document in line with the concept of 'fair dealing' under the Copyright, Designs and Patents Act 1988 (?)
- Users may not further distribute the material nor use it for the purposes of commercial gain.

Where a licence is displayed above, please note the terms and conditions of the licence govern your use of this document.

When citing, please reference the published version.

### Take down policy

While the University of Birmingham exercises care and attention in making items available there are rare occasions when an item has been uploaded in error or has been deemed to be commercially or otherwise sensitive.

If you believe that this is the case for this document, please contact [UBIRA@lists.bham.ac.uk](mailto:UBIRA@lists.bham.ac.uk) providing details and we will remove access to the work immediately and investigate.

# 1 Estimation of river flow using CubeSats remote sensing

2  
3 Adriano M. Junqueira <sup>a,b\*</sup>, Feng Mao <sup>c</sup>, Tatiana S. G. Mendes <sup>d</sup>, Silvio J. C. Simões <sup>e</sup>,

4 José A. P. Balestieri <sup>a</sup>, David M. Hannah <sup>b</sup>

5 <sup>a</sup> São Paulo State University (UNESP), School of Engineering, Guaratinguetá - Brazil

6 <sup>b</sup> University of Birmingham, School of Geography, Earth and Environmental Sciences, Birmingham –  
7 United Kingdom

8 <sup>c</sup> Cardiff University, School of Earth and Environmental Sciences, Cardiff - United Kingdom

9 <sup>d</sup> São Paulo State University (UNESP), Institute of Science and Technology, São José dos Campos – Brazil

10 <sup>e</sup> University of the Algarve, Centre for Marine and Environmental Research, Algarve - Portugal

11  
12 \*Corresponding author:

13 Email: [adriano.junqueira@unesp.br](mailto:adriano.junqueira@unesp.br) (A. M. Junqueira)

14 Av. Dr. Ariberto Pereira da Cunha, 333 – Guaratinguetá – SP – Brazil – Zipcode: 12516-410

## 16 **Abstract:**

17  
18 River flow characterizes the integrated response from watersheds, so it is essential to quantify to  
19 understand the changing water cycle and underpin the sustainable management of freshwaters.  
20 However, river gauging stations are in decline with ground-based observation networks shrinking.  
21 This study proposes a novel approach of estimating river flows using the Planet CubeSats  
22 constellation with the possibility to monitor on a daily basis at the sub-catchment scale through  
23 remote sensing. The methodology relates the river discharge to the water area that is extracted  
24 from the satellite image analysis. As a testbed, a series of Surface Reflectance PlanetScope images  
25 and observed streamflow data in Araguaia River (Brazil) were selected to develop and validate  
26 the methodology. The study involved the following steps: (1) survey of measurements of water  
27 level and river discharge using in-situ data from gauge-based Conventional Station (CS) and  
28 measurements of altimetry using remote data from JASON-2 Virtual Station (JVS); (2) survey of

29 Planet CubeSat images for dates in step 1 and without cloud cover; (3) image preparation  
30 including clipping based on different buffer areas and calculation of the Normalized Difference  
31 Vegetation Index (NDVI) per image; (4) water bodies areas calculation inside buffers in the Planet  
32 CubeSat images; and (5) correlation analysis of CubeSat water bodies areas with JVS and CS  
33 data. Significant correlations between the water bodies areas with JVS ( $R^2 = 88.83\%$ ) and CS ( $R^2$   
34  $= 96.49\%$ ) were found, indicating that CubeSat images can be used as a CubeSat Virtual Station  
35 (CVS) to estimate the river flow. This newly proposed methodology using CubeSats allows for  
36 more accurate results than the JVS-based method used by the Brazilian National Water Agency  
37 (ANA) at present. Moreover, CVS requires small areas of remote sensing data to estimate with  
38 high accuracy the river flow and the height variation of the water in different timeframes. This  
39 method can be used to monitor sub-basin scale discharge and to improve water management,  
40 particularly in developing countries where the presence of conventional stations is often very  
41 limited.

42

#### 43 **Highlights:**

44

- 45 • Use of remote sensing information from Planet CubeSats constellation to build and assess a  
46 methodology to river flow estimation;
- 47 • This method has significant opportunity for river flow estimation at ungauged sites at the daily  
48 and sub-basin scales;
- 49 • The improvement of river flow measurements is essential to understand the changing water  
50 cycle and underpin the sustainable management of freshwaters.

51

52 **Keywords:** River flow; CubeSat; Remote Sensing; Cerrado (Savannah); Change Detection;  
53 Spatiotemporal Resolution.

54

55

## 56 **1 Introduction**

57

58 Freshwater is a basic requirement for life but the knowledge of river flow rates is scarce  
59 (Gleason and Smith, 2014). A better understanding of the large-scale water cycle process is  
60 essential to underpin socio-economic development and sustainably manage water-dependent  
61 ecosystems (Döll et al., 2014; Hannah et al., 2011; Kingston et al., 2020). River flow characterizes  
62 the integrated hydrological response and water yield from watersheds. Nowadays, there is a clear  
63 decline of river gauging stations and a shrinking of ground-based observation networks (Dixon et  
64 al., 2020; Hannah et al., 2011).

65 Conventional gauging stations are well developed and have contributed to quantify the  
66 movement of water in river channels. However, conventional stations are not enough to determine  
67 more complex riverine environments that involve the movement of water over wetlands and  
68 floodplains in multiple channel types (Lettenmaier, 2007), requiring new multidisciplinary  
69 approaches to improve the observation networks.

70 The advances in remote sensing hydrology, particularly over the past 10 years, have  
71 demonstrated that hydraulic variables can be measured reliably from orbiting satellite platforms  
72 (Huang et al., 2018). As the deluge of big data continues to impact practically every commercial  
73 and scientific domain, geosciences have also witnessed a major revolution from being a data-poor  
74 field to a data-rich field (Karpatne et al., 2019; Reichstein et al., 2019). The use of remote sensing  
75 by satellite for streamflow analyses can be categorized into techniques based on satellite altimetry,  
76 Synthetic Aperture Radar (SAR), and optical images (Ahmad and Kim, 2019).

77 To accurately detect river flow regimes at a field scale from space, a new high spatial and  
78 temporal resolution remote sensing source is necessary to improve water- level time series  
79 (Bogning et al., 2018). While satellites such as Sentinel-2 and Landsat may have an adequate  
80 spatial resolution for different applications (Sadeh et al., 2019), their temporal resolution (5 and  
81 16 days revisit time, respectively) is not ideal for detection of flow regimes changes, as there may  
82 be weeks between the acquisition of two clear-sky images (Houborg and McCabe, 2018a).

83 Applications of satellite remote sensing in hydrological surface water modelling, mapping,  
84 and parameter estimation were reported in some reviews based on Earth Observing Systems  
85 (Huang et al., 2018; Joshi et al., 2016; Musa et al., 2015; Wagner et al., 2018) mainly using SAR,  
86 optical, altimetry and DEM data. Focusing flow river estimation, different techniques were  
87 applied to estimate the river width by averaging multiple cross-sections over an area (Gleason  
88 and Smith, 2014), use the Synthetic Aperture Radar (SAR) to calculate water area (Ahmad and  
89 Kim, 2019), and fusion topography dataset (Anh and Aires, 2019; Moramarco et al., 2019). The  
90 spatiotemporal restrictions for using remote sensing satellite data have been partly overcome via  
91 multisensor data fusion (Houborg and McCabe, 2018b) but all solutions proposed can not be  
92 replicated for daily measurements at a high spatial resolution.

93 Thus, remote sensing has the potential of conducting rapid, cost-effective, and continuous  
94 surveys of river management practices over large scales. Notably, the constellations of micro or  
95 nano-satellites, known as CubeSats, are revolutionizing the high spatiotemporal resolution  
96 possibilities in remote sensing and can potentially be used to capture many observations over time  
97 (Sadeh et al., 2019) and monitor dynamics surface water changes (Cooley et al., 2019, 2017). The  
98 repetitive observation mechanism of multiples CubeSats enables studying the river dynamics and  
99 observe different physical properties (Marinho et al., 2020). Among the different Cubesats on orbit,  
100 the CubeSat constellation provided by Planet Labs Inc. has the advantage of providing a near-  
101 daily revisit time globally at 3-meter orthorectified spatial resolution. It is also worth noting that  
102 Remote Sensing (RS) has several methods and techniques to identify land and water areas  
103 considering bands variation of different multi-spectral images (Acharya et al., 2018). Index  
104 methods are mostly used to estimate surface water that separates the water from the background  
105 based on a threshold value. Among these indexes, Normalized Difference Vegetation Index  
106 (NDVI) and Normalized Difference Water Index (NDWI) are frequently adopted as they include  
107 visible and Near Infrared (NIR) bands provided by satellite optical images (Elsahabi et al., 2016).

108 The aims of this study were (1) to develop an innovative methodology for semi-automated  
109 river flow estimation using visible and NIR from Planet CubeSats bands to detect changes in the  
110 surface of flood area and (2) to compare Planet CubeSats derived river flow with Conventional

111 flow meters Station (CS) and JASON (Joint Altimetry Satellite Oceanography Network) Virtual  
112 gauging Station (JVS). The Araguaia River, in the Cerrado biome of Brazil, was selected as the  
113 research area.

114

## 115 **2. Description of the study area**

116

117 The Tocantins-Araguaia hydrographic region, with a total area of 920,087 km<sup>2</sup> and 13,779  
118 m<sup>3</sup>/s of average discharge (Brasil/ANA, 2015), is the most important fluvial system draining the  
119 tropical savannah ecoregion of Brazil (Cerrado biome). Some areas of this region have been  
120 affected by severe water scarcity events since 2012 (Naturatins, 2017). In general terms, the  
121 hydrologic regime depends on the dominant climate (tropical wet-dry) with floods from January  
122 to May (rain period) and low water between June to September. This region is the confluence of  
123 two major rivers: the Tocantins River (~1,960 km extension) and the Araguaia River (~2,600 km  
124 extension). The Araguaia sub-basin (around 386,765 km<sup>2</sup>) represents around 42% of the  
125 hydrographic region and along its path, is placed the largest river island in the world, Bananal  
126 Island (Figure 1).

127

128 *Figure 1*

129

130 The Araguaia River is one of the priority areas for conservation of the aquatic biodiversity of  
131 the Cerrado biome and has been the target of political and environmental debates due to the  
132 intense and indiscriminate expansion of agricultural activities, with a greater degradation of the  
133 natural environment during the last four decades (Latrubesse and Stevaux, 2006). The entire sub-  
134 basin has just 166 conventional river gauging stations for an area of 386,765 km<sup>2</sup> and more than  
135 6,000 river stretches mapped.

136 This region needs to be better monitored due to the increase in intensive agriculture and the  
137 use of water (Althoff et al., 2020). Especially in the Araguaia River, the irrigated area increased

138 more than 116% between 2006 and 2012, and the cultivated area increased by about 20% in the  
139 same period (ANA, 2015). In the last decade, the Araguaia sub-basin has been suffering from  
140 water scarcity in several tributaries of the Araguaia river, obliging managers to take actions for  
141 rationing the water use in agriculture to prioritize human and animal supply (Lauris, 2019;  
142 Naturatins, 2017).

143 As a testbed to develop and validate the proposed methodology, two river gauging stations  
144 that are calibrated by ANA and used as an official instrument for public policies in this region  
145 were selected. One of the rivers gauging stations was the in-situ Conventional Station (CS) ID  
146 26350000 (<http://gestorpcd.ana.gov.br>) managed by ANA, located in São Felix do Araguaia –  
147 MT (11°37'8.6" S; 50°39'75.0" W – WGS84 Datum). This station employs an instrument for  
148 monitoring the river flow for 24/7 hours with records registered every 15 minutes. The other river  
149 gauging station was the JASON-2 Virtual Station (JVS) ID 1055S05036WO  
150 (<http://hidrosat.ana.gov.br>), which is monitored by ANA in cooperation with Institut de  
151 Recherche pour le Développement (IRD) with barycenter data at 10°54'42.0" S; 50°36'48.6" W  
152 – WGS84 Datum. This station acquires altimetry information by satellite to monitor the water  
153 level and derived river flow, with no equipment locally installed. The JVS dataset is related to the  
154 average altitude of all available altimetry data, along the JASON-2 track, over the river area in  
155 each satellite cycle. JVS observations occur every 9.9 days from the JASON-2 satellite in the  
156 same ground track within a margin of  $\pm 1$  km (CNES; NASA, 2011).

157 The detailed characteristics of both selected stations are shown in Figure 2. The distance  
158 between the CS and JVS is relatively close with 78 km (Euclidean distance) allowing their  
159 comparison with the proposed methodology.

160

161

*Figure 2*

162

163

### 164 3. Data and Methods

165  
166 For this study, the available Planet CubeSat data was explored to establish an innovative  
167 method for estimating river flow based on daily remote sensing images.

#### 168 169 3.1. CubeSat data

170  
171 This study used Planet images to develop a flow estimation model. These images are captured  
172 by Planet using an approach based on ‘fast design’ to launch satellites, mission control and  
173 operations systems, and the development of a web-based platform for imagery processing and  
174 delivery ([www.planet.com](http://www.planet.com)). Planet is a commercial satellite operator that enhanced observation  
175 capacity offered by constellations of small and standardized satellites and employs an “always-  
176 on” image-capturing method (Planet Team, 2020).

177 This CubeSat constellation consists of 130 small-satellites at an altitude of approximately 475  
178 km, following each other on two near-polar orbits of roughly 8° (descendent orbit) and 98°  
179 (ascendent orbit) inclination respectively, imaging the Earth at local morning time (Planet Team,  
180 2020). The distance along the orbit between the CubeSats is constructed such that the longitudinal  
181 progression between them over the rotating Earth leads to the scan of the surface. Thus, the full  
182 constellation provides daily sun-synchronous coverage of the entire Earth (except the polar hole)  
183 with the resolution of 3.7 meters at nadir (Ground Sample Distance), 12-bit radiometric  
184 resolution, and 4 spectral bands (Blue [455 - 515 nm], Green [500 - 590 nm], Red [590 - 670 nm]  
185 and Near-InfraRed [780 - 860 nm]) (Planet Team, 2020).

186 The CubeSat across-track off-nadir viewing angle used for imaging usually to be lower than  
187 5° (Planet Team, 2020) reducing the complexity to evaluate bands’ variation of different multi-  
188 spectral images arising from environmental noise such as shadow, however, these CubeSat do not  
189 present some spectral bands as Middle Infrared (MIR) and Shortwave Infrared (SWIR), used in  
190 different indexes applied to water such as TCW, MNDWI, NDWI, AWEI (Elsahabi et al., 2016).



191 The images can be downloaded from the Planet portal (<https://www.planet.com/explorer>) and  
192 include three types of raster images: (a) digital number (DN) commonly represented by an  
193 uncalibrated image into physically meaningful units; (b) top of atmosphere reflectance (TOA)  
194 that is the reflectance measured by a space-based sensor flying higher than the earth's atmosphere  
195 (calibrated to a radiance image), and (c) surface reflectance (SR) that is the radiance image  
196 atmospherically corrected and ready to be used to extract quantitative information about features  
197 on the Earth surface. As SR reflects the difference among land covers more accurately than other  
198 remotely sensed measurements (Huang et al., 2018). In this study, it was used the SR image  
199 products, orthorectified with 3 meters spatial resolution, positional accuracy with less than 10-  
200 meters Root Mean Square Error (RMSE) suitable for analytic and visual applications.

201

### 202 *3.2. A method for estimating river flows using CubeSats*

203

204 This study was divided into five steps: (1) survey of measurements of water level and  
205 river discharge using in-situ data from gauge-based Conventional Station (CS) and measurements  
206 of altimetry using remote data from JASON-2 Virtual Station (JVS); (2) preparation of river  
207 section and buffers and survey of CubeSat images for selected dates (correlated with step 1 and  
208 without cloud cover); (3) image preparation, including clipping based on different buffer areas  
209 followed by NDVI calculation per image, and data processing over CS and JVS stations using  
210 Extract-Transform-Load (ETL); (4) water bodies areas calculation inside buffer for river flow  
211 estimation in the Planet CubeSat images; and (5) correlation analysis of CubeSat water bodies  
212 areas with JVS and CS data (Figure 3).

213

214

### *Figure 3*

215

216 Firstly, the CS and JVS measurements were collected in the period of 01/01/2018 to  
217 30/07/2018, a period that historically includes the greatest variation in the flow of this river over  
218 the years. The dataset for CS included the water level and river flow every 15 minutes. The JVS

219 were collected altimetry data in repetitive periods of 10 days according to the measures provided  
220 by the altimetry missions satellite. The use of JVS data was independent of the time of collection  
221 and resulted in a median of 11:03 a.m. local time.

222 In the second step, a cross-section of the river was used as a reference for creating side buffers  
223 with 50, 250, 500, and 1000 meters. This cross-section was determined nearby to the JASON's  
224 tracking to provide better conditions of comparison between the virtual stations and these buffers  
225 sections were created to reduce the satellite image processing area in the water surface calculation.  
226 Using the location of these buffers, Planet CubeSat images were searched for all dates with JVS  
227 data. The CubeSat images search also included the completed cover of buffer areas, the absence  
228 of clouds, and the possibility of using the surface reflectance product (SR) as input (Table 1).

229 In the third step, each image downloaded from the Planet portal was clipped on the buffer  
230 areas and processed to calculate the Normalized Difference Vegetation Index (NDVI) with a scale  
231 ranging from -1 to 1. The NDVI was calculated using the Red and Near-InfraRed regions of the  
232 electromagnetic spectrum with Equation 1 since these satellites do not have yet more specific  
233 spectral bands for the development of more sophisticated methods. For each image analyzed, the  
234 river flood areas were classified with NDVI values lower than 0.15.

235

$$236 \quad NDVI = \frac{(NIR\ Band - Red\ Band)}{(NIR\ Band + Red\ Band)} \quad (1)$$

237

238 In the fourth step, the water bodies' areas were calculated for all clipped buffers in the dates  
239 analyzed, resulting in a temporal table of flooding areas. Then, in the fifth step, we performed the  
240 regression curves (exponential, linear, logarithmic, polynomial, power-law, and moving  
241 averages) between the water bodies areas for 4 different buffers (50, 250, 500, and 1000 m) and  
242 the 3 sets of reference data (JVS - altimetry, CS - water level, CS - flow). After that, 12 different  
243 Pearson coefficients ( $R^2$ ) were determined according to the best-fitted regression curves. The  
244 relationship between  $R^2$  and the four buffer areas were analyzed for each set of reference data,

245 determining the equation used to predict the river flow from the CubeSat image flood area, which  
246 represented the CubeSat Virtual Station (CVS).

247

#### 248 **4 Results**

249

250 The data collected from CS showed a river flow ranging from 868 to 4,739 m<sup>3</sup>/s and a water  
251 level varying from 328 to 710 cm for the entire monitoring period in the Araguaia basin. A  
252 significant relationship between the river flow and the water level measurements ( $R^2=1$ ) was  
253 found (Figure 4a). Concerning the JVS data, altimetry values between 177.9 to 181.1 m were  
254 observed, with a good correlation to CS water level ( $R^2= 0.85$ ) (Figure 4b).

255

256 *Figure 4*

257

258 In the survey of Planet CubeSat images, 8 image dates were selected with CS and JVS  
259 correspondent data, completed cover the buffer areas, absence of clouds, and available surface  
260 reflectance product (SR) (Table 1).

261

262 *Table 1*

263

264 In these 8 images, water bodies areas ranging from 39,924 to 54,846 m<sup>2</sup> for buffer 50 m, from  
265 173,313 to 276,984 m<sup>2</sup> for buffer 250 m, from 320,805 to 557,586 m<sup>2</sup> for buffer 500 m, and from  
266 563,895 to 1,097,469 m<sup>2</sup> for buffer 1000 m were determined (Table 2). Considering the maximum  
267 values of water bodies in each buffer, it was verified that the flood area corresponds to 77.3%,  
268 63.9%, 52.5%, and 37.7%, respectively, for the 50 m, 250 m, 500 m, and 1000 m buffer areas.

269

270 *Table 2*

271

272 Based on the water bodies areas determined in each buffer area, the regression models were  
273 performed as demonstrated in Figure 5. Due to the obtained data values and its measure of  
274 greatness, the river flow equation was adjusted to the power-law regression model, while the  
275 water level and altimetry equations were adjusted to linear regression models.

276

277 *Figure 5*

278

279 Considering the results obtained in the regression models, it was found that the buffer of 500  
280 m was the lowest buffer area capable of providing a high Pearson's coefficient that remained  
281 stable even with the increase of buffer area (Figure 6). Therefore, the buffer of 500 m was selected  
282 to be the CVS and to estimate the river flow.

283

284 *Figure 6*

285

286 To estimate the river flow ( $Q_e$ ), water level ( $L_e$ ) and altimetry ( $A_e$ ) were determined the  
287 Equations 2 ( $R^2 = 96.49\%$ ), 3 ( $R^2 = 94.38\%$ ) and 4 ( $R^2 = 88.83\%$ ) respectively; in which  $A_{f500r}$   
288 is the flooding area ( $m^2$ ) in the 500 m buffer.

289

$$290 \quad Q_e = 10^{-13} \cdot A_{f500r}^{2.8737} \quad (2)$$

291

$$292 \quad L_e = 0.0015 \cdot A_{f500r} - 161.56 \quad (3)$$

293

$$294 \quad A_e = 10^{-5} \cdot A_{f500r} + 175.14 \quad (4)$$

295

296 Equation 5 is the root mean square error (RMSE) that represents the accuracy estimator and,  
297 the precision estimator given by the standard deviation (SD) (Equation 6), were also determined  
298 for Equations 2, 3, and 4. The results related to RMSE and SD are present in Table 3.

299

$$RMSE = \sqrt{\sum_{n=1}^n \frac{(Reference_n - Calculated_n)^2}{n}} \quad (5)$$

301

$$SD = \sqrt{\sum_{n=1}^n \frac{[(Reference_n - Calculated_n) - \overline{(Reference_n - Calculated_n)}]^2}{n-1}} \quad (6)$$

303

304

### *Table 3*

305

306 In summary, this CVS methodology established for the Araguaia river can be explored to  
307 estimate the river flow, water level, and altimetry for other rivers around the world.

308

## 309 **5 Discussion**

310

311 Hydrographic data obtained from satellites and other remote sources provide the possibility  
312 of broad global coverage for river discharge estimates (Bahadur and Samuels, 2013; Lakshmi,  
313 2004). The advances in computing power and data storage capacity associated with the  
314 innovations in the satellite remote sensing area are enabling global monitoring of different  
315 variables related to the water cycle (Lettenmaier et al., 2015; Wagner et al., 2018). Nowadays,  
316 the increase in the number of Planet CubeSats brings images with more cost-effective and higher  
317 spatiotemporal resolutions than other commercial satellites (Houborg and McCabe, 2018b).

318 Currently, Planet CubeSat is the only commercial constellation available for capturing daily  
319 optical images with high resolution of the entire surface of the Earth. In Brazil, there is a national  
320 program (<https://www.gov.br/mj/pt-br/aceso-a-informacao/acoes-e-programas/programa-brasil-mais/>) that provides Planet images with high-resolution (3 m orthorectified per pixel) freely  
321 available to governmental institutions throughout the Brazilian territory.

323 Access to the CubeSat images is an important political and economic decision. The use of  
324 satellite information is an economical way of measuring river discharge using in situ gauges  
325 stations that are costly to install, maintain, and operate (Zaji et al., 2018). According to U.S.

326 Geological Survey (USGS), the cost for a typical in situ gauge station evolves several costs  
327 associated with its activities, which are estimated at 41% for labour staff (field and office), 25%  
328 for administrative activities, 10% for building and utilities, 10% for field equipment, 7% for data  
329 management and delivery, 5% for vehicles and 2% for travel (Norris, 2010). These percentages  
330 can vary according to location and conditions, especially in remote areas where in situ gauges  
331 stations require expensive field works (Norris, 2010). Besides reducing costs, the implementation  
332 of technology-based remote sensing for river discharge can avoid exposing surveyors to  
333 dangerous and reacher inaccessible rivers (Samboko et al., 2020).

334 Monitoring of rivers requires a reliable system, being the water level and the river discharge  
335 the two essential parameters in this analysis (Mao et al., 2020, 2019, 2018; Mostafavi, 2018).  
336 Besides that, the monitoring requires integrated modelling tools that cover adequate spatial and  
337 temporal scales involving mathematical applications (Mannschatz et al., 2015). In this context,  
338 an innovative methodology for river flow estimation was developed using Planet CubeSat images  
339 to detect changes in the flood area surface, which can be used as a CubeSat Virtual Station (CVS).

340 Although methods of river discharge from the direct measurement of width, depth, and  
341 velocity (based on velocity-area method) provides a higher level of accuracy than orbital remote  
342 sensing (Bjerkli et al., 2005), the proposed methodology used an approach that relies on  
343 identifying of the water surface from morphologic features that are easier to recognize from space.  
344 The geomorphic features and structural dynamics related to river discharge as channel type,  
345 channel slope, channel roughness, depth, and velocity were assumed associated with the river  
346 hydraulic geometries and can be used to develop more robust calibration methods.

347 The CVS data obtained were compared with the measures of water level and river discharge  
348 of a Conventional Station (CS) and altimetry of the JASON Virtual Sation (JVS), located in the  
349 Araguaia River (Brazil).

350 Analyzing the CS data collected in this study, it was found a complete correlation ( $R^2 = 1$ )  
351 between the measurements of water level and river discharge, indicating that the in-situ reference  
352 station used was well-calibrated. It was also observed a high correlation of the CS water level  
353 measurements with the JVS altimetry data ( $R^2 = 0.85$ ) confirming that the satellite remote sensing

354 can be a useful tool for river flow estimation. Bogning et al., (2018) also found a good correlation  
355 ( $R^2 > 0.82$ ) when in-situ gauge records were compared to altimetry- based water levels from  
356 multiple satellites, composed of a network of altimetric virtual station (ENVISAT, SARAL,  
357 ERS- 2, Sentinel- 3A, JASON- 2, and JASON- 3 data). This analysis was performed in the  
358 Ogooué river basin, located at Gabon, with an annual river discharge of 4,750 m<sup>3</sup>/s and a  
359 hydrologic wet-dry regime similar to the characteristics of this study in the Araguaia River. Smith  
360 and Pavelsky, (2008) demonstrated that remotely sensed width variations were well correlated to  
361 ground measurements of river discharge ( $R^2 = 0.81$ ) when taken days later and hundreds of  
362 kilometres downstream. Gleason and Smith (2014) showed that useful estimates of absolute river  
363 discharge may be obtained solely from river width using multiple satellite Landsat images,  
364 through a characteristic scaling law named At-Many-station Hydraulic Geometry (AMHG), with  
365 no ground-based or a priori information. The AMHG was calculated with the monitoring of large  
366 extensions (10 to 13 km) from remote sensing along the river.

367 JVS and Landsat can be employed in the case of lacking river rating curves and cross-  
368 sectional geometries, as well as when the water levels or flow rates measurements are missing in  
369 situ station historic data. However, the use of JVS and Landsat data in a river hydrodynamics  
370 context is limited by data coverage in both time and space, which may be insufficient to capture  
371 key spatiotemporal variations in water surface elevation daily (Houborg and McCabe, 2018a).  
372 Besides that, JVS can be used only to monitor the level of wider rivers (Huang et al., 2018) that  
373 intersect with JASON-2 satellite tracks.

374 In this study, the innovative method using Planet CubeSat images provides a possibility to  
375 monitor river narrower than those evaluated by JVS and Landsat due to its higher spatial  
376 resolution (Houborg and McCabe, 2018b, 2018a). Also, Planet constellation allows monitoring  
377 rivers around the world (Kääb et al., 2019) with more flexibility to establish Virtual Stations  
378 concerning JVS that are limited to the track satellite intersections. The fact of use high-resolution  
379 Planet CubeSat images, with low acquisition inclination, reduces the effect of shadow and  
380 increases the river border identification details. This agrees with Bjerklie et al. (2003), who  
381 reinforces that even if the river could always be distinguished from the surrounding landscape,

382 narrower channels would have greater uncertainty in the width estimates due to the relative width  
383 concerning the resolution of the sources. The altimetry accuracy for the JVS stations varies with  
384 the river width, with better precision the wider the channels (Bjerklie et al., 2018), while for the  
385 proposed CVS stations the accuracy in determining the level varies with the flooded area close to  
386 the station, with precision dependent on the slope at the edges of the channel, as it reflects in the  
387 expansion of the flooded area.

388 For the period of study, 8 images were selected with dates correspondent to CS and JVS  
389 reference measures. However, many other Planet CubeSat images were available in the period,  
390 with 110 cloud-free SR images against 22 JVS measures, representing at least 5 times more  
391 information than JVS data for the Araguaia river. Although many Planet images were available,  
392 it was decided to use only the images that allowed the comparison with CS and JVS on the same  
393 date.

394 The data from CubeSat images showed a well-correlated estimation with river discharge  
395 ( $R^2 = 96.49\%$ ) when small lengths of the river (500 m buffer) were analyzed. This correlation was  
396 higher than the JVS data and river discharge correlation ( $R^2=85.01\%$ ) that is one of reference  
397 adopted by the ANA in Brazil. The results using CubeSat images were also well correlated with  
398 CS water level ( $R^2 = 94.38\%$ ) and JVS altimetry ( $R^2 = 88.83\%$ ) when evaluated the flooding area  
399 ( $m^2$ ). According to Papa et al. (2010), ideally, the goal for discharge data accuracy is within  $\pm 5\%$   
400 related to the true value, but the community agrees that 15% to 20% accuracy is in general  
401 acceptable for discharge measurements.

402 Virtual stations with CubeSat images showed greater accuracy and precision at lower river  
403 discharge rates whereas JASON virtual stations have greater accuracy and precision for higher  
404 river discharge rates. This is observed by the fact that in the CVS, a better refinement of the  
405 flooded area is possible even with the presence of sandbanks while the JVS presents greater noise  
406 in the identification of the altimetry related to these areas. At higher river discharges, we observed  
407 that the JVS presented better details of the altimetry, especially when the increase in the level of  
408 the river occurred inside the channel without accompanying the expansion of the flooded area.



409 In this study, it was visually observed a refined design of the flooded areas due to the  
410 resolution of the CubeSat images. From this observation, an attempt was made to find a  
411 relationship between the width of the river and a buffer size that provided less demand of image  
412 areas to achieve a high Pearson coefficient. It was observed that a buffer ranging from 0.5 to 1  
413 times the average width of the studied river section allowed to reach these results, remaining  
414 stable even the value of  $R^2$ . Then, the proposed methodology allows the use of less than 388 km<sup>2</sup>  
415 of images/year for this virtual station, representing an advantage in comparison with the AMGH  
416 methodology, which suggests the evaluation of multiple river widths by stretches greater than 10  
417 km. Using 3-meter Planet images as reference, Pôssa et al. (2018) observed a slightly increased  
418 precision in the water surface delineation compared to Landsat and Sentinel images due to spatial  
419 resolution of satellite images.

420 Overall, these experiments allow us to employ a simple exponential equation model with  
421 daily CubeSat images for well predict the river flow at a monthly scale, based on the surface  
422 hydrological information measured from space as proof of concept and utility of the method. The  
423 use of new constellations, new hydrological science methods, and advancements in resolutions  
424 (spatial, temporal, and radiometric) of remote sensing make possible the application of monitoring  
425 increasingly smaller watersheds, as they have coverage of several pixels and more frequent data  
426 acquisitions (Lakshmi, 2004). Besides that, to flow estimation measurement, the CubeSat images  
427 can be used to study other processes related to data assimilation; flood monitoring and prediction;  
428 floodplain connectivity (Cooley et al., 2017); land surface characteristics (land use, temperature,  
429 snow cover) (Reichle, 2008); image fusion to land use mapping and monitoring (Houborg and  
430 McCabe, 2018b; Joshi et al., 2016); and water quality monitoring (Maciel et al., 2020).

431

## 432 **6 Conclusion**

433

434 An innovative method for semi-automated river flow estimation using Planet CubeSat data  
435 was developed to detect changes in the surface of the flood area, using the Araguaia River as a  
436 testbed. In summary, the flood areas detected by CubeSat data showed significant correlations  
437 with river discharge and water level measurements from gauge-based Conventional Station (CS)  
438 in small areas of the river using a reduced amount of satellite images. CubeSat data also presented  
439 a significant correlation with altimetry measurements from JASON-2 Virtual Station (JVS)  
440 officially adopted by the Brazilian agency, with the advantage to provides greater records  
441 numbers per year, more flexibility of position for Virtual Stations establishment, and the  
442 possibility to monitor narrower rivers. The river discharge extracted from Cubesat data showed a  
443 higher correlation with CS than JVS, indicating that CVS had more capacity of reproducing the  
444 ground truth compared to JVS.

445 In the future, this method can be completely automated to fill the gaps in the streamflow  
446 series, to compute different riverine contributions in the sub-basin, and to promote an  
447 understanding of river discharge spatial distribution on a near-real-time for entire continents. This  
448 method can also be used as a cost-effective alternative to monitoring the sub-basin discharges,  
449 improving water management, particularly, in developing countries where the presence of  
450 conventional stations is limited.

## 451 **Acknowledgements**

452

453 The authors are grateful to Brazilian National Water Agency (ANA – Agência Nacional de  
454 Águas) for providing the fluvial data in Brazil (conventional and virtual stations) and, to  
455 SCCON/PLANET data images accessed from the online portal  
456 (<https://www.planet.com/explorer>).

457 This study was financed in part by the Coordenação de Aperfeiçoamento de Pessoal de Nível  
458 Superior - Brasil (CAPES) - Finance Code 001.

459 Adriano M. Junqueira was hosted at the University of Birmingham, UK, to undertake this work.  
460 Jose Antonio Perrella Balestieri is grateful to the Conselho Nacional de Desenvolvimento  
461 Científico e Tecnológico (CNPq), process 301853/2018-5.

## 462 **References**

463

464 Acharya, T.D., Subedi, A., Lee, D.H., 2018. Evaluation of water indices for surface water extraction in a  
465 Landsat 8 scene of Nepal. *Sensors (Switzerland)* 18, 1–15. <https://doi.org/10.3390/s18082580>

466 Ahmad, W., Kim, D., 2019. Estimation of flow in various sizes of streams using the Sentinel-1 Synthetic  
467 Aperture Radar (SAR) data in Han River Basin, Korea. *Int. J. Appl. Earth Obs. Geoinf.* 83, 101930.  
468 <https://doi.org/10.1016/j.jag.2019.101930>

469 Althoff, D., Rodrigues, L.N., David, D., 2020. Impacts of climate change on the evaporation and  
470 availability of water in small reservoirs in the Brazilian savannah. *Clim. Chang.* 18.

471 Anh, D.T.L., Aires, F., 2019. River discharge estimation based on satellite water extent and topography:  
472 An application over the Amazon. *J. Hydrometeorol.* 20, 1851–1866. [https://doi.org/10.1175/JHM-](https://doi.org/10.1175/JHM-D-18-0206.1)  
473 [D-18-0206.1](https://doi.org/10.1175/JHM-D-18-0206.1)

474 Bahadur, R., Samuels, W.B., 2013. Application of Remote Sensing and Satellite Imagery for Hydrologic  
475 Modeling [WWW Document]. *Environ. Water Resour. Inst.* URL  
476 [http://message.asce.org/LP=205?utm\\_campaign=EWRI-20130429-](http://message.asce.org/LP=205?utm_campaign=EWRI-20130429-EWRI+Currents+Spring+2013&utm_medium=email)  
477 [EWRI+Currents+Spring+2013&utm\\_medium=email](http://message.asce.org/LP=205?utm_campaign=EWRI-20130429-EWRI+Currents+Spring+2013&utm_medium=email) (accessed 1.17.21).

478 Bjerklie, D.M., Birkett, C.M., Jones, J.W., Carabajal, C., Rover, J.A., Fulton, J.W., Garambois, P.A.,  
479 2018. Satellite remote sensing estimation of river discharge : Application to the Yukon River  
480 Alaska. *J. Hydrol.* 561, 1000–1018. <https://doi.org/10.1016/j.jhydrol.2018.04.005>

481 Bjerklie, D.M., Dingman, S.L., Vorosmarty, C.J., Bolster, C.H., Congalton, R.G., 2003. Evaluating the  
482 potential for measuring river discharge from space 278, 17–38. [https://doi.org/10.1016/S0022-](https://doi.org/10.1016/S0022-1694(03)00129-X)  
483 [1694\(03\)00129-X](https://doi.org/10.1016/S0022-1694(03)00129-X)

484 Bjerklie, D.M., Moller, D., Smith, L.C., Dingman, S.L., 2005. Estimating discharge in rivers using  
485 remotely sensed hydraulic information. *J. Hydrol.* 309, 191–209.  
486 <https://doi.org/10.1016/j.jhydrol.2004.11.022>

487 Bogning, S., Frappart, F., Blarel, F., Niño, F., Mahé, G., Bricquet, J.P., Seyler, F., Onguéné, R., Etamé, J.,

488 Paiz, M.C., Braun, J.J., 2018. Monitoring water levels and discharges using radar altimetry in an  
489 ungauged river basin: The case of the Ogooué. *Remote Sens.* 10.  
490 <https://doi.org/10.3390/rs10020350>

491 Brasil/ANA, 2015. Conjuntura dos recursos hídricos no Brasil: regiões hidrográficas brasileiras.

492 Cooley, S.W., Smith, L.C., Ryan, J.C., Pitcher, L.H., Pavelsky, T.M., 2019. Arctic-Boreal Lake  
493 Dynamics Revealed Using CubeSat Imagery. *Geophys. Res. Lett.* 46, 2111–2120.  
494 <https://doi.org/10.1029/2018GL081584>

495 Cooley, S.W., Smith, L.C., Stepan, L., Mascaro, J., 2017. Tracking dynamic northern surface water  
496 changes with high-frequency planet CubeSat imagery. *Remote Sens.* 9, 1–21.  
497 <https://doi.org/10.3390/rs9121306>

498 Dixon, H., Sandström, S., Cudennec, C., Lins, H.F., Abrate, T., Bérod, D., Chernov, I., Ravalitera, N.,  
499 Sighomnou, D., Teichert, F., 2020. Intergovernmental cooperation for hydrometry—what, why and  
500 how? *Hydrol. Sci. J.* 00, 1–15. <https://doi.org/10.1080/02626667.2020.1764569>

501 Döll, P., Jiménez-Cisneros, B., Oki, T., Arnell, N.W., Benito, G., Cogley, J.G., Jiang, T., Kundzewicz,  
502 Z.W., Mwakalila, S., Nishijima, A., 2014. Integrating risks of climate change into water  
503 management. *Hydrol. Sci. J.* 60, 4–13. <https://doi.org/10.1080/02626667.2014.967250>

504 Elshahi, M., Negm, A., Hamid M.H. El Tahan, A., 2016. Performances Evaluation of Surface Water  
505 Areas Extraction Techniques Using Landsat ETM+ Data: Case Study Aswan High Dam Lake  
506 (AHD). *Procedia Technol.* 22, 1205–1212. <https://doi.org/10.1016/j.protcy.2016.02.001>

507 Gleason, C.J., Smith, L.C., 2014. Toward global mapping of river discharge using satellite images and at-  
508 many-stations hydraulic geometry. *Proc. Natl. Acad. Sci. U. S. A.* 111, 4788–4791.  
509 <https://doi.org/10.1073/pnas.1317606111>

510 Hannah, D.M., Demuth, S., van Lanen, H.A.J., Looser, U., Prudhomme, C., Rees, G., Stahl, K.,  
511 Tallaksen, L.M., 2011. Large-scale river flow archives: Importance, current status and future needs.  
512 *Hydrol. Process.* 25, 1191–1200. <https://doi.org/10.1002/hyp.7794>

513 Houborg, R., McCabe, M.F., 2018a. A Cubesat enabled Spatio-Temporal Enhancement Method  
514 (CESTEM) utilizing Planet, Landsat and MODIS data. *Remote Sens. Environ.* 209, 211–226.  
515 <https://doi.org/10.1016/j.rse.2018.02.067>

516 Houborg, R., McCabe, M.F., 2018b. Daily retrieval of NDVI and LAI at 3 m resolution via the fusion of  
517 CubeSat, Landsat, and MODIS data. *Remote Sens.* 10. <https://doi.org/10.3390/rs10060890>

518 Huang, C., Chen, Y., Zhang, S., Wu, J., 2018. Detecting, Extracting, and Monitoring Surface Water From  
519 Space Using Optical Sensors: A Review. *Rev. Geophys.* 56, 333–360.  
520 <https://doi.org/10.1029/2018RG000598>

521 Joshi, N., Baumann, M., Ehammer, A., Fensholt, R., Grogan, K., Hostert, P., Jepsen, M.R., Kuemmerle,  
522 T., Meyfroidt, P., Mitchard, E.T.A., Reiche, J., Ryan, C.M., 2016. A Review of the Application of  
523 Optical and Radar Remote Sensing Data Fusion to Land Use Mapping and Monitoring 1–23.  
524 <https://doi.org/10.3390/rs8010070>

525 Kääh, A., Altena, B., Mascaro, J., 2019. River-ice and water velocities using the Planet optical cubesat  
526 constellation. *Hydrol. Earth Syst. Sci.* 23, 4233–4247. <https://doi.org/10.5194/hess-23-4233-2019>

527 Karpatne, A., Ebert-Uphoff, I., Ravela, S., Babaie, H.A., Kumar, V., 2019. Machine Learning for the  
528 Geosciences: Challenges and Opportunities. *IEEE Trans. Knowl. Data Eng.* 31, 1544–1554.  
529 <https://doi.org/10.1109/TKDE.2018.2861006>

530 Kingston, D.G., Massei, N., Dieppois, B., Hannah, D.M., Hartmann, A., Lavers, D.A., Vidal, J.P., 2020.  
531 Moving beyond the catchment scale: Value and opportunities in large-scale hydrology to  
532 understand our changing world. *Hydrol. Process.* 34, 2292–2298. <https://doi.org/10.1002/hyp.13729>

533 Lakshmi, V., 2004. Use of Satellite Remote Sensing in, in: *International Journal*. Istanbul.

534 Latrubesse, E.M., Stevaux, J.C., 2006. Características físico-bióticas e problemas ambientais associados à  
535 planície aluvial do Rio Araguaia - Brasil Central. *Rev. UnG - Geociências* 5, 65–73.

536 Lauris, P., 2019. Comitê pede ao Naturatins a suspensão das outorgas de captação de água na Bacia do  
537 Rio Formoso [WWW Document]. *J. do Tocantins*. URL  
538 [https://www.jornaldotocantins.com.br/editorias/vida-urbana/comitê-pede-ao-naturatins-a-](https://www.jornaldotocantins.com.br/editorias/vida-urbana/comitê-pede-ao-naturatins-a-suspensão-das-outorgas-de-captação-de-água-na-bacia-do-rio-formoso-1.1875921)  
539 [suspensão-das-outorgas-de-captação-de-água-na-bacia-do-rio-formoso-1.1875921](https://www.jornaldotocantins.com.br/editorias/vida-urbana/comitê-pede-ao-naturatins-a-suspensão-das-outorgas-de-captação-de-água-na-bacia-do-rio-formoso-1.1875921) (accessed  
540 2.14.20).

541 Lettenmaier, D.P., 2007. Measuring Surface Water From Space. *Rev. Geophys.* 45, 1–24.  
542 <https://doi.org/10.1029/2006RG000197.1>.INTRODUCTION

543 Lettenmaier, D.P., Alsdorf, D., Dozier, J., Huffman, G.J., Pan, M., Wood, E.F., 2015. Inroads of remote  
544 sensing into hydrologic science during the Water Resources Research era. *J. Am. Water Resour.*  
545 *Assoc.* 5, 2–2. <https://doi.org/10.1111/j.1752-1688.1969.tb04897.x>

546 Maciel, D.A., Márcia, E., Moraes, L. De, Barbosa, C.F., Martins, V.S., Júnior, R.F., Oliveira, H.,  
547 Augusto, L., Carvalho, S. De, Lobo, F.D.L., 2020. Evaluating the potential of CubeSats for remote

548 sensing reflectance retrieval over inland waters. *Int. J. Remote Sens.* 41, 2807–2817.  
549 <https://doi.org/10.1080/2150704X.2019.1697003>

550 Mannschatz, T., Wolf, T., Hülsmann, S., 2015. Nexus Tools Platform : Web-based comparison of  
551 modelling tools for analysis of water-soil-waste nexus *Environmental Modelling & Software Nexus*  
552 Tools Platform : Web-based comparison of modelling tools for analysis of water-soil-waste nexus.  
553 *Environ. Model. Softw.* 76, 137–153. <https://doi.org/10.1016/j.envsoft.2015.10.031>

554 Mao, F., Clark, J., Buytaert, W., Krause, S., Hannah, D.M., 2018. Water sensor network applications:  
555 Time to move beyond the technical? *Hydrol. Process.* 32, 2612–2615.  
556 <https://doi.org/10.1002/hyp.13179>

557 Mao, F., Khamis, K., Clark, J., Krause, S., Buytaert, W., Ochoa-Tocachi, B.F., Hannah, D.M., 2020.  
558 Moving beyond the Technology: A Socio-technical Roadmap for Low-Cost Water Sensor Network  
559 Applications. *Environ. Sci. Technol.* 54, 9145–9158. <https://doi.org/10.1021/acs.est.9b07125>

560 Mao, F., Khamis, K., Krause, S., Clark, J., Hannah, D.M., 2019. Low-Cost Environmental Sensor  
561 Networks: Recent Advances and Future Directions. *Front. Earth Sci.*  
562 <https://doi.org/10.3389/feart.2019.00221>

563 Marinho, C.S., Sacramento, V., Cangiano, M.R., Cicerelli, R.E., Almeida, T., 2020. Accumulated  
564 Reflectance Technique for Sampling Delimitation in the Riacho Fundo Creek, Lago Paranoá-Df,  
565 from Planetscope Images. 2020 IEEE Lat. Am. GRSS ISPRS Remote Sens. Conf. LAGIRS 2020 -  
566 Proc. XLII, 259–263. <https://doi.org/10.1109/LAGIRS48042.2020.9165645>

567 Moramarco, T., Barbetta, S., Bjerklie, D.M., Fulton, J.W., Tarpanelli, A., 2019. River Bathymetry  
568 Estimate and Discharge Assessment from Remote Sensing. *Water Resour. Res.* 55, 6692–6711.  
569 <https://doi.org/10.1029/2018WR024220>

570 Mostafavi, M., 2018. River Monitoring Over Amazon and Danube Basin Using Multi- Mission Satellite  
571 Radar Altimetry. *J. Hydrogeol. Hydrol. Eng. Res.* 7:2, 16. [https://doi.org/10.4172/2325-  
572 9647.1000167](https://doi.org/10.4172/2325-9647.1000167)

573 Musa, Z.N., Popescu, I., Mynett, A., 2015. C:\Users\adriano.junqueira\Documents\Adriano  
574 2021\Doutorado\Artigos Acessados\2018 - A Review on Applications of Remote Sensing and  
575 Geographic Information Systems (GIS) in Water Resources and Flood Risk Management.pdf for  
576 surface water modelling, mapping . *Hydrol. Earth Syst. Sci.* 19, 3755–3769.  
577 <https://doi.org/10.5194/hess-19-3755-2015>

578 Naturatins, 2017. Portaria Naturatins 300. Diário Of. do Estado do Tocantins - Bras. 45.

579 Norris, J.M., 2010. U. S. Geological Survey Streamgage Operation and Maintenance Cost Evaluation  
580 (No. Fact Sheet 2010-3025).

581 Planet Team, 2020. Planet Imagery Product Specifications - June 2020. San Francisco.

582 Pôssa, É.M., Maillard, P., Gomes, M.F., Silva, I., Leão, G., 2018. On water surface delineation in rivers  
583 using Landsat-8, Sentinel-1 and Sentinel-2 data, in: SPIE Remote Sensing 2018 - Remote Sensing  
584 for Agriculture, Ecosystems, and Hydrology. Berlin, p. 45. <https://doi.org/10.1117/12.2325725>

585 Reichle, R.H., 2008. Data assimilation methods in the Earth sciences. *Adv. Water Resour.* 31, 1411–  
586 1418. <https://doi.org/10.1016/j.advwatres.2008.01.001>

587 Reichstein, M., Camps-Valls, G., Stevens, B., Jung, M., Denzler, J., Carvalhais, N., Prabhat, 2019. Deep  
588 learning and process understanding for data-driven Earth system science. *Nature* 566, 195–204.  
589 <https://doi.org/10.1038/s41586-019-0912-1>

590 Sadeh, Y., Zhu, X., Chenu, K., Dunkerley, D., 2019. Sowing date detection at the field scale using  
591 CubeSats remote sensing. *Comput. Electron. Agric.* 157, 568–580.  
592 <https://doi.org/10.1016/j.compag.2019.01.042>

593 Samboko, H.T., Abas, I., Luxemburg, W.M.J., Savenije, H.H.G., Makurira, H., Banda, K., Winsemius,  
594 H.C., 2020. Evaluation and improvement of remote sensing-based methods for river flow  
595 management. *Phys. Chem. Earth* 117, 102839. <https://doi.org/10.1016/j.pce.2020.102839>

596 Smith, L.C., Pavelsky, T.M., 2008. Estimation of river discharge, propagation speed, and hydraulic  
597 geometry from space : Lena River, Siberia 44, 1–11. <https://doi.org/10.1029/2007WR006133>

598 Wagner, W., Lucieer, A., Houborg, R., Verhoest, N.E.C., 2018. The Future of Earth Observation in  
599 Hydrology. *Hydrol Earth Syst Sci* 21, 3879–3914. <https://doi.org/10.5194/hess-21-3879-2017>.The

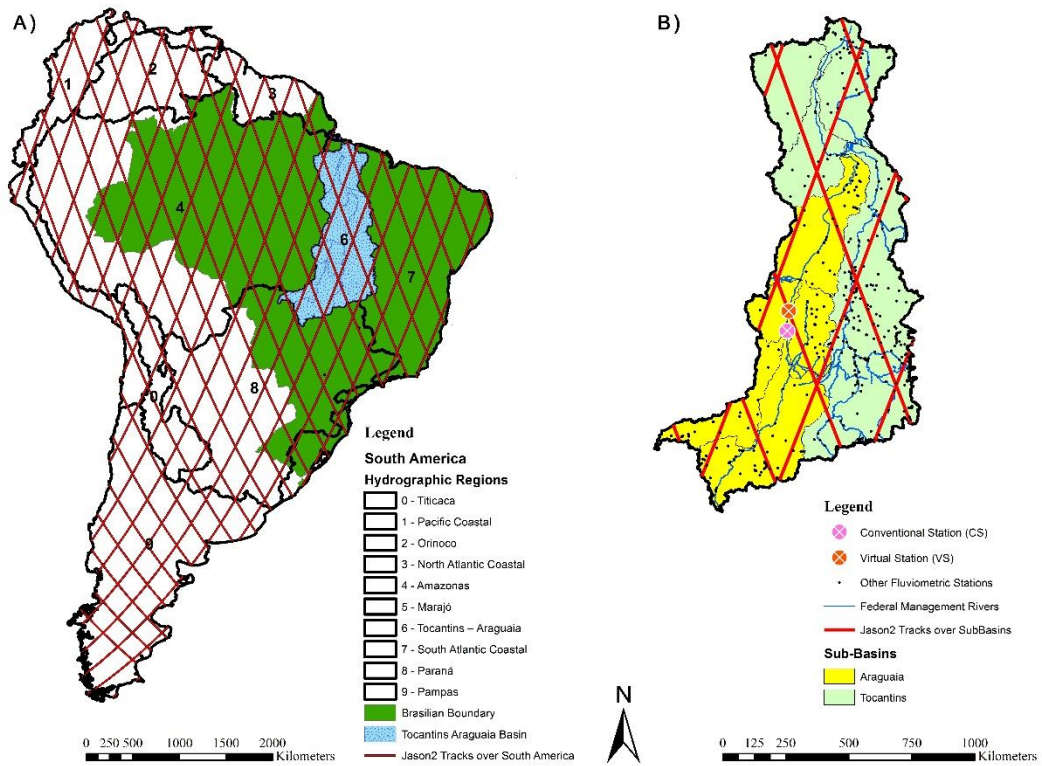
600 Zaji, A.H., Bonakdari, H., Gharabaghi, B., 2018. Remote Sensing Satellite Data Preparation for  
601 Simulating and Forecasting River Discharge. *IEEE Trans. Geosci. Remote Sens.* 56, 3432–3441.  
602 <https://doi.org/10.1109/TGRS.2018.2799901>

603

604 **Figures**

605

606 **Fig. 1.** Overview of the study area. (A) Overview of South America with its 10 Hydrographic Regions  
607 (black), passes of JASON-2 over the area (red) and, the Tocantins-Araguaia basin (light blue); (B) Zoom  
608 in the Tocantins (light-green) - Araguaia (yellow) basin boundaries, presence of rivers with federal  
609 regulation (blue) and all fluviometric in situ stations (black dots), complemented by tracks of Jason-2 (red)  
610 highlighting JVS (red circle; north) and CS (pink circle; south) ground references.

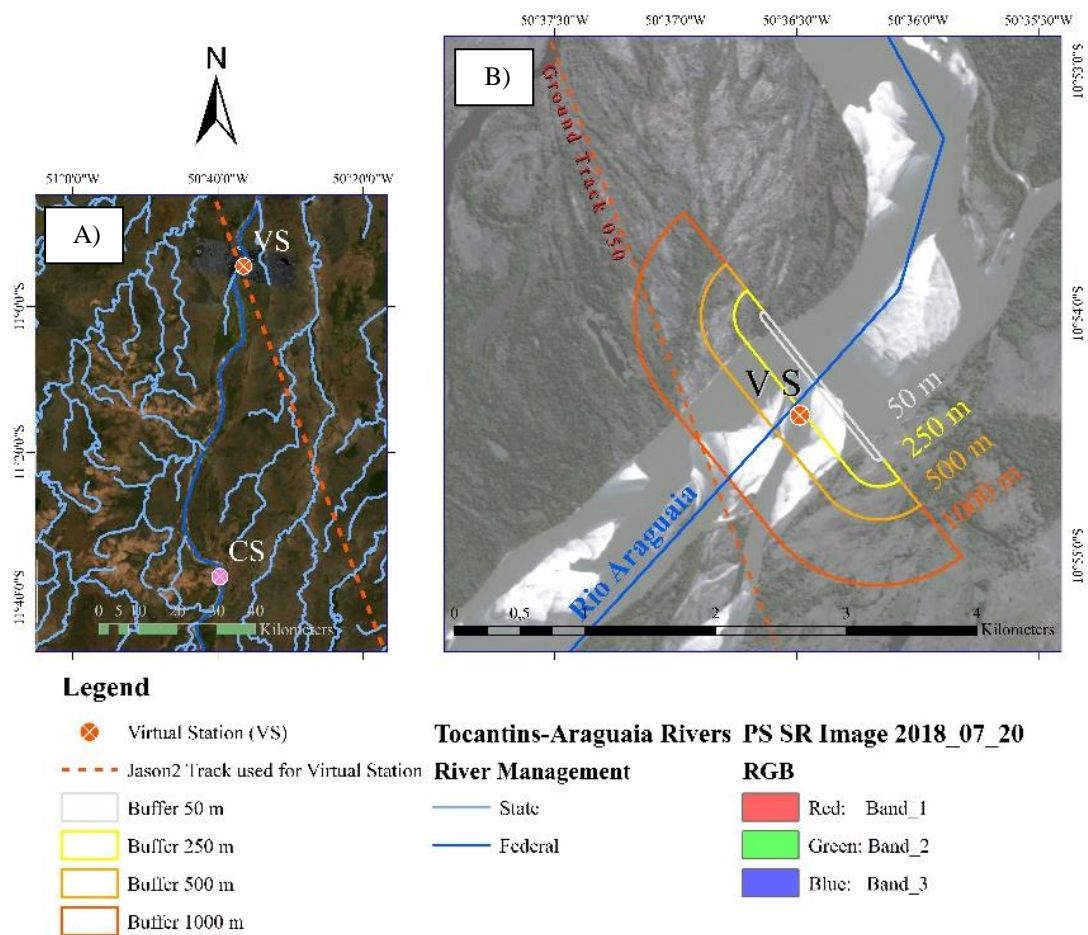


611

612



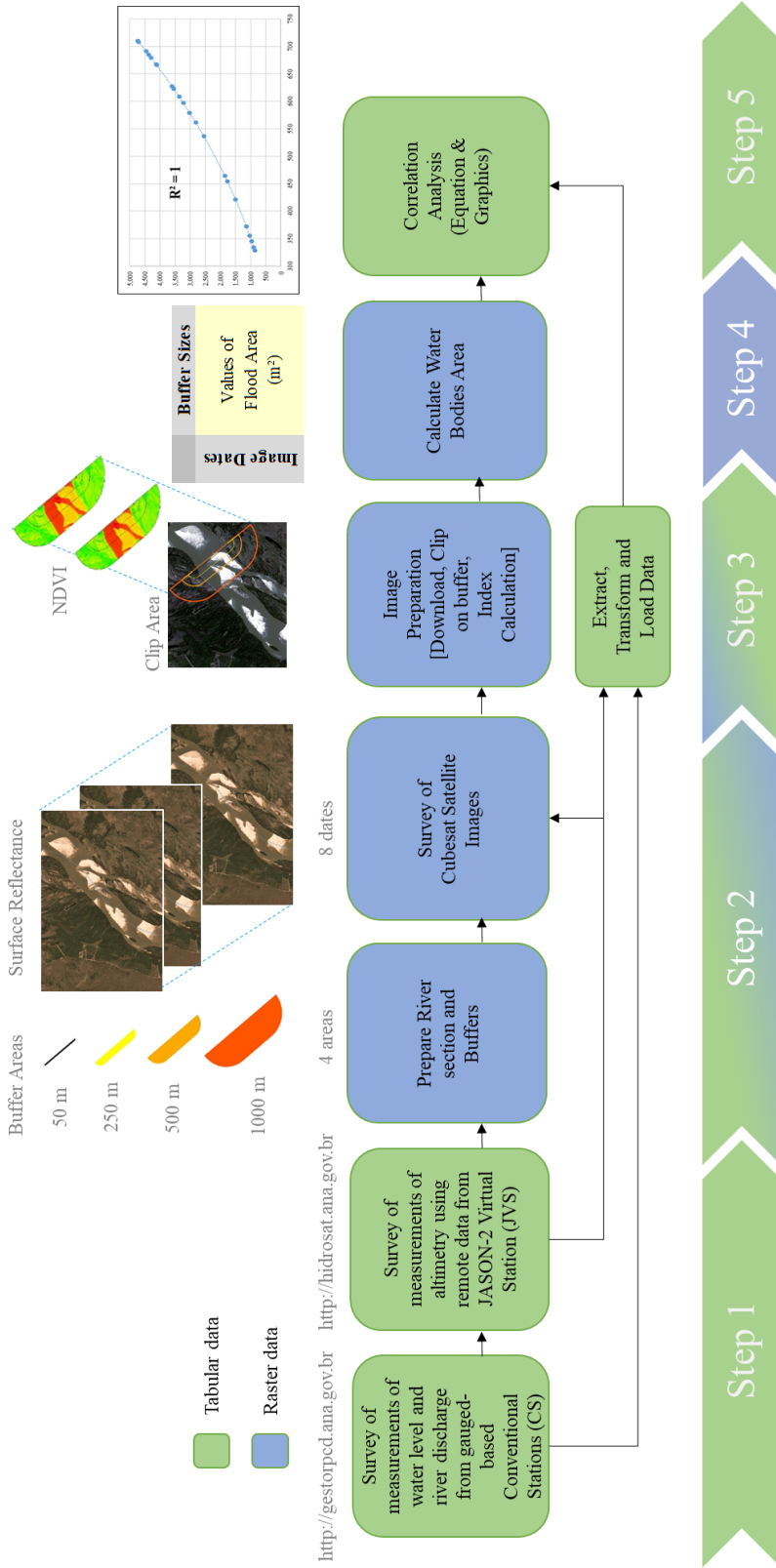
613 **Fig. 2.** The study area of the Araguaia sub-basin. (A) Zoom in the Araguaia River (center) highlighting the  
 614 track of Jason-2 (red) over the surface drainage (blue), and the Conventional Station (CS) used as ground  
 615 truth (pink dot). The region where the Jason-2 track crosses the Araguaia River is the Virtual Station (JVS)  
 616 far 78 km from CS and, the region used to download the CubeSat SR images; (B) Zoom in the VS (red dot)  
 617 over the Araguaia River (blue line) with the 4 different buffer areas used in the methodology (50 m – grey;  
 618 250 m – yellow; 500 m – orange; 1000 m – red). In the background it is presented the Surface Reflectance  
 619 (SR) Planet image from July, 20<sup>th</sup> 2018 with 50% transparency and the representation of the Jason-2 track  
 620 over the region (red dashed line).  
 621



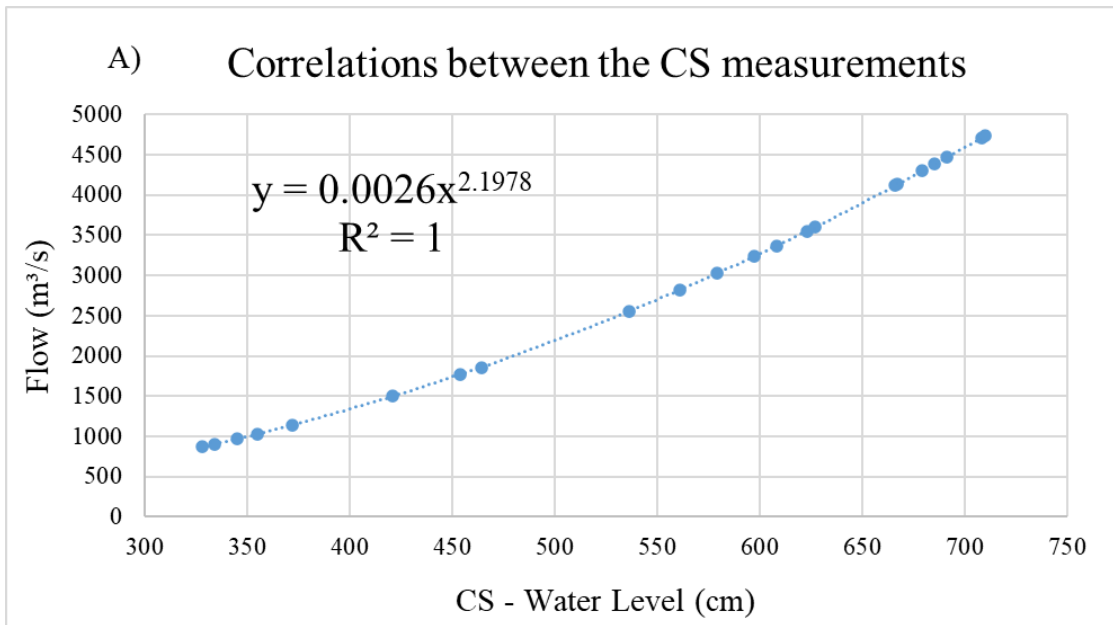
622

623

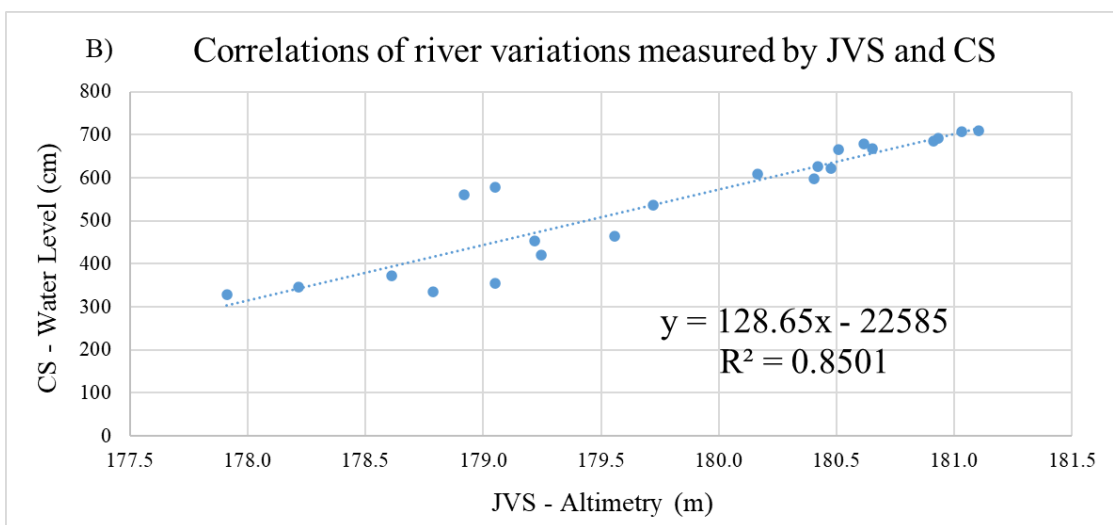
624 **Fig. 3.** Methodological framework using CubeSat to estimate the river flow. The 1<sup>st</sup> step is used for  
625 gathering reference information to support the key-curves. In the 2<sup>nd</sup> step are prepared the specific buffer  
626 areas and selected the CubeSat images to investigate the correlation between inundation extent and river  
627 flow. The 3<sup>rd</sup> step is used for preprocessing selected CubeSat images with pixel classification (water/no-  
628 water) based on NDVI values. In the 4<sup>th</sup> step are calculated the flooding area for each image. The last step  
629 is to evaluate the regression analysis comparing the 3 reference data (CS - Flow river; CS – Water Level;  
630 JVS – Altimetry).



632 **Fig. 4.** Evaluation of the reference data. **(a)** Relationship between the river level (x-axis) and flow (y-axis)  
 633 by the CS in the São Felix do Araguaia/MT station for the period of analyses. The blue curve represents  
 634 the exponential equation ( $y = 0.0026x^{2.1978}$ ) that are well adjusted with  $R^2 = 1$ .  
 635 **(b)** Relationship between the altitudes (x-axis) calculated by the JVS and the quotes determined on the  
 636 water level (y-axis) by the CS in the Araguaia basin for the period of analyses. The blue curve represents  
 637 the linear equation ( $y = 128.65x - 22585$ ) with  $R^2 = 0.8501$ . In both figures, the solid blue circles represent  
 638 correlated values with 10 days interval.  
 639



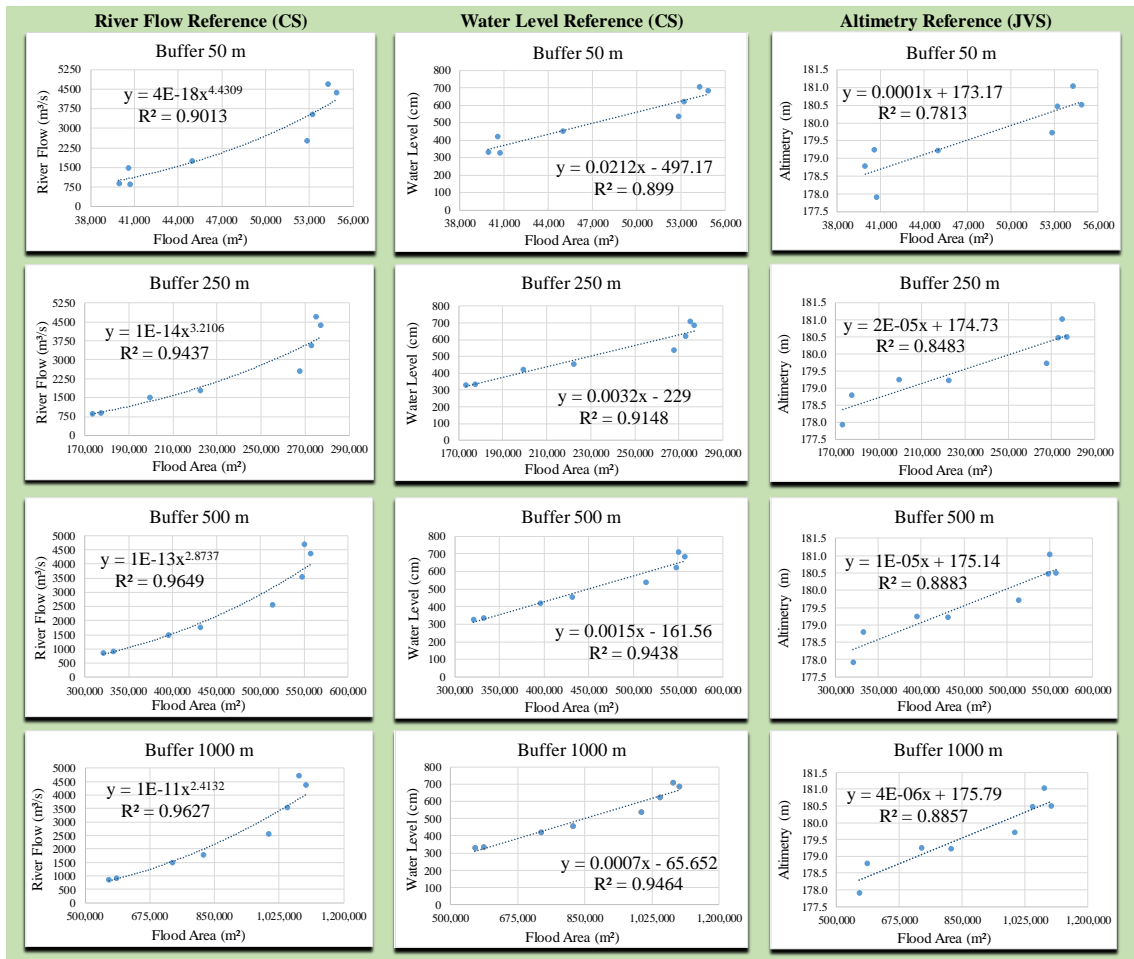
640  
 641



642

643 **Fig. 5.** Regression curves against 3 ground references and 4 different buffer sizes

644

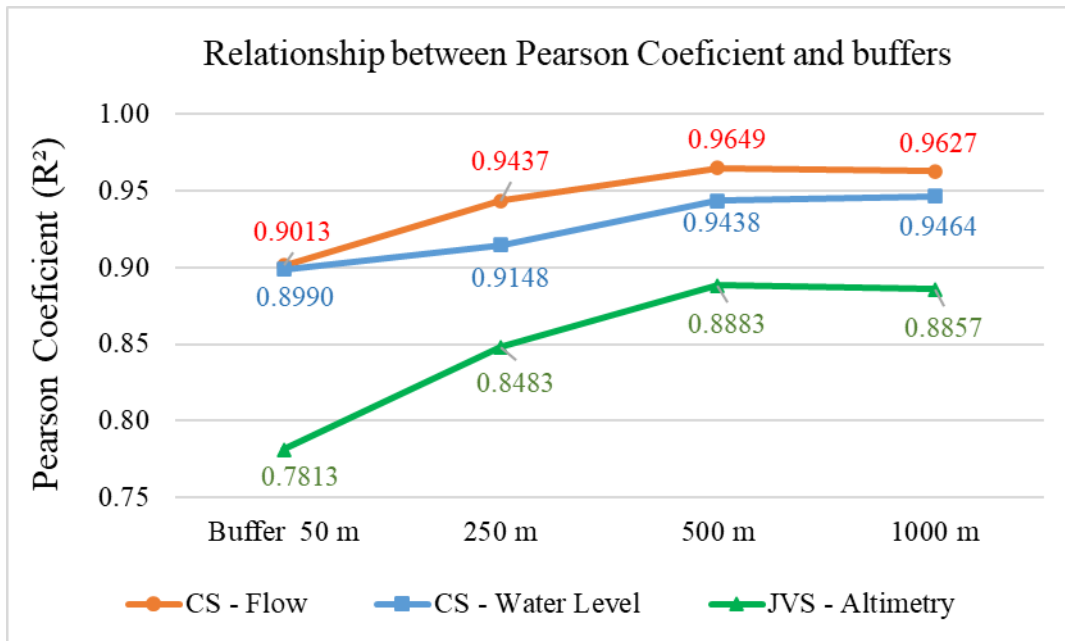


645

646

647 **Fig. 6.** Relationship between  $R^2$  (x-axis) and 4 buffers distances (y-axis) for 3 sets of reference data (CS  
648 water level and river flow and JVS altimetry).

649



650

651

652 **Tables**

653

654 **Table 1.** Detail of measurements related to JVS, CS, and satellite images used in the period of analysis  
 655 for river flow estimates.

656

| Label<br>ID | Date       | JASON                                     | Conventional                        | Conventional                                      | Surface Reflectance              |
|-------------|------------|---|-------------------------------------|---|----------------------------------|
|             |            | Virtual<br>Station (JVS)<br>Altimetry (m) | Station (CS)<br>Water Level<br>(cm) | Station (CS)<br>River Flow<br>(m <sup>3</sup> /s) | (SR)<br>Planet CubeSat<br>Images |
| 1           | 2018 01 03 | 179.049                                   | 579                                 | 3,022.10  | incomplete/cloud                 |
| 2           | 2018 01 13 | 178.917                                   | 561                                 | 2,819.00  | incomplete/cloud                 |
| 3           | 2018 01 23 | 180.478                                   | 623                                 | 3,551.62  | available                        |
| 4           | 2018 02 02 | 180.404                                   | 597                                 | 3,233.03  | incomplete/cloud                 |
| 5           | 2018 02 12 | 180.165                                   | 608                                 | 3,365.81  | incomplete/cloud                 |
| 6           | 2018 02 22 | 180.615                                   | 679                                 | 4,294.38  | incomplete/cloud                 |
| 7           | 2018 03 04 | 181.030                                   | 708                                 | 4,709.77  | available                        |
| 8           | 2018 03 13 | 181.103                                   | 710                                 | 4,739.20  | incomplete/cloud                 |
| 9           | 2018 03 23 | 180.913                                   | 685                                 | 4,378.59  | incomplete/cloud                 |
| 10          | 2018 04 02 | 180.931                                   | 691                                 | 4,463.70  | incomplete/cloud                 |
| 11          | 2018 04 12 | 180.651                                   | 667                                 | 4,128.66  | incomplete/cloud                 |
| 12          | 2018 04 22 | 180.508                                   | 666                                 | 4,115.01  | available                        |
| 13          | 2018 05 02 | 180.419                                   | 627                                 | 3,602.11  | incomplete/cloud                 |
| 14          | 2018 05 12 | 179.721                                   | 536                                 | 2,549.77  | available                        |
| 15          | 2018 05 22 | 179.557                                   | 464                                 | 1,856.67  | TOA image                        |
| 16          | 2018 06 01 | 179.220                                   | 454*                                | 1,769.96*   | available                        |
| 17          | 2018 06 11 | 179.248                                   | 421                                 | 1,499.74  | available                        |
| 18          | 2018 06 21 | 178.612                                   | 372                                 | 1,143.57  | TOA image                        |

|           |            |         |     |          |                  |
|-----------|------------|---------|-----|----------|------------------|
| <b>19</b> | 2018 07 01 | 179.049 | 355 | 1,032.33 | incomplete/cloud |
| <b>20</b> | 2018 07 10 | 178.217 | 345 | 969.81   | incomplete/cloud |
| <b>21</b> | 2018 07 20 | 178.786 | 334 | 903.52   | available        |
| <b>22</b> | 2018 07 30 | 177.912 | 328 | 868.46   | available        |

\* average between 02/06/2018 and 31/05/2018

657

| <b>Label ID</b> | <b>Date</b> | <b>JASON Virtual Station (JVS) Altimetry (m)</b> | <b>Conventional Station (CS) Water Level (cm)</b> | <b>Conventional Station (CS) River Flow (m<sup>3</sup>/s)</b> | <b>Surface Reflectance (SR) Planet CubeSat Images</b> |
|-----------------|-------------|--|---|---|---|
| <b>1</b>        | 2018 01 03  | 179.049  | 579   | 3,022.10  | incomplete/cloud                                      |
| <b>2</b>        | 2018 01 13  | 178.917  | 561   | 2,819.00  | incomplete/cloud                                      |
| <b>3</b>        | 2018 01 23  | 180.478  | 623   | 3,551.62  | available   |
| <b>4</b>        | 2018 02 02  | 180.404  | 597   | 3,233.03  | incomplete/cloud                                      |
| <b>5</b>        | 2018 02 12  | 180.165  | 608   | 3,365.81  | incomplete/cloud                                      |
| <b>6</b>        | 2018 02 22  | 180.615  | 679   | 4,294.38  | incomplete/cloud                                      |
| <b>7</b>        | 2018 03 04  | 181.030  | 708   | 4,709.77  | available   |
| <b>8</b>        | 2018 03 13  | 181.103  | 710   | 4,739.20  | incomplete/cloud                                      |
| <b>9</b>        | 2018 03 23  | 180.913  | 685   | 4,378.59  | incomplete/cloud                                      |
| <b>10</b>       | 2018 04 02  | 180.931  | 691   | 4,463.70  | incomplete/cloud                                      |
| <b>11</b>       | 2018 04 12  | 180.651  | 667   | 4,128.66  | incomplete/cloud                                      |
| <b>12</b>       | 2018 04 22  | 180.508  | 666   | 4,115.01  | available   |
| <b>13</b>       | 2018 05 02  | 180.419  | 627   | 3,602.11  | incomplete/cloud                                      |
| <b>14</b>       | 2018 05 12  | 179.721  | 536   | 2,549.77  | available   |
| <b>15</b>       | 2018 05 22  | 179.557  | 464   | 1,856.67  | TOA image   |
| <b>16</b>       | 2018 06 01  | 179.220  | 454*  | 1,769.96*   | available   |
| <b>17</b>       | 2018 06 11  | 179.248  | 421   | 1,499.74  | available   |
| <b>18</b>       | 2018 06 21  | 178.612  | 372   | 1,143.57  | TOA image   |
| <b>19</b>       | 2018 07 01  | 179.049  | 355   | 1,032.33  | incomplete/cloud                                      |
| <b>20</b>       | 2018 07 10  | 178.217  | 345   | 969.81  | incomplete/cloud                                      |
| <b>21</b>       | 2018 07 20  | 178.786  | 334   | 903.52  | available   |
| <b>22</b>       | 2018 07 30  | 177.912  | 328   | 868.46  | available   |

\* average between 02/06/2018 and 31/05/2018

658



659 **Table 2.** Flood area calculated inside buffers with NDVI value smaller than 0.15.

660

| Label<br>ID | Selected dates of<br>Surface Reflectance (SR)<br>Planet CubeSat Images | Flood Area            | Flood Area             | Flood Area             | Flood Area              |
|-------------|--|-----------------------|------------------------|------------------------|-------------------------|
|             |  | inside                | inside                 | inside                 | inside                  |
|             |  | Buffer                | Buffer                 | Buffer                 | Buffer                  |
|             |  | 50m (m <sup>2</sup> ) | 250m (m <sup>2</sup> ) | 500m (m <sup>2</sup> ) | 1000m (m <sup>2</sup> ) |
| 3           | 2018 01 23   | 53.181                | 273.024                | 547.929                | 1,046,745               |
| 7           | 2018 03 04   | 54.261                | 275.040                | 550.251                | 1,079.640               |
| 12          | 2018 04 22   | 54.846                | 276.984                | 557.586                | 1,097,469               |
| 14          | 2018 05 12   | 52.839                | 267.615                | 513.891                | 997.580                 |
| 16          | 2018 06 01   | 44.964                | 222.336                | 431.730                | 819.477                 |
| 17          | 2018 06 11   | 40.572                | 199.512                | 395.604                | 736.335                 |
| 21          | 2018 07 20   | 39.924                | 177.471                | 332.415                | 585.909                 |
| 22          | 2018 07 30   | 40.707                | 173.313                | 320.805                | 563.895                 |

661

662 **Table 3.** Accuracy (*RMSE*) and precision (*SD*) estimators related to river flow (*Qe*), water level (*Le*) and  
 663 altimetry (*Ae*)  
 664

| <b>Regression Curves</b>  | <b>Accuracy Estimator (<i>RMSE</i>)</b> | <b>Precision Estimator (<i>SD</i>)</b> | <b>Unit</b>       |
|---------------------------|---|--|-------------------|
| River Flow ( <i>Qe</i> )  | 717,59                                  | 553,63                                 | m <sup>3</sup> /s |
| Water Level ( <i>Le</i> ) | 59,45                                   | 37,16                                  | cm                |
| Altimetry ( <i>Ae</i> )   | 0,33                                    | 0,34                                   | m                 |

665